Journal of Inorganic and Organometallic Polymers and Materials (2021) 31:1323–1335
https://doi.org/10.1007/s10904-020-01805-1

Electrical, and Magnetic Characteristics of Homo- and Hetero-Bimetallic Macromolecular Complexes with π-Conjugated Imine-oxime Backbone

Isam M. Arafa[1] · Mazin Y. Shatnawi[1] · Ruba M. Al-Equr[1]

Received: 9 August 2020 / Accepted: 26 October 2020 / Published online: 2 November 2020

Abstract
Seven homo- and hetero-bimetallic macromolecular complexes (BMCs) were prepared via an *in-situ* multi-step complexation reaction of Cu^{II}, Ni^{II} and Fe^{III} metal centers with imine- oxime π-conjugated ditropic spacer (1,4-phenylene-bis(2,3-butanedeimineoxime, L^{2-}). The structures of the obtained $[M\text{-}L_2\text{-}M]_x$, $[M`\text{-}L_2\text{-}M`]_x$, $[M\text{-}L_2\text{-}M`]_x$ and their μ-oxo-$[M\text{-}L_2\text{-}Fe]_x$ BMCs (M = $Cu^{II}$, $Ni^{II}$; M` = Fe^{III}) were elucidated using different spectroscopic (UV–Vis, FT-IR), powder X-ray diffraction (p-XRD) and microscopic (SEM) techniques. The SEM images indicate that the obtained BMCs exhibit nano/micro globular and rod-like textures. The electrical and magnetic characteristics of the obtained BMCs can be described as magneto-semiconducting materials. The structural, electrical, and magnetic properties inherited in the prepared regime demonstrate that the examined semiconducting π-spacer has clear ability to semi-conduct electron transport and delocalize spin leading to antiferromagnetic coupling, thus offering a favorable magnetic exchange pathway between the paramagnetic metal sites. However, ferromagnetic enhancement is observed in the μ-oxo-$[M\text{-}L_2\text{-}Fe]_x$ BMCs where the μ-oxo-bridge overplays the role of the π-spacer. A magnetic responsive thin film was conveniently obtained by solvent casting of the μ-oxo-$[Ni\text{-}L_2\text{-}Fe]_x$ BMC in a transparent poly(methamethylacrylate) matrix.

Keywords Imine-oxime · Photo-magnetism · Macromolecular complexes · π-spacer · Multi-functional material · Thin films

1 Introduction

Recent progress in the field of multi-functional materials has shown that metal–organic based materials play an important role in the development of electrochromic, electromagnetic, optoelectronic and spintronic systems [1–25]. The incorporation of metal centers into discrete, supramolecular ensembles, and polymeric organic architectures permit their exploitation in a wide variety of stimulus-responsive devices. The interplay between electronic charge transfer and spin-delocalization in semiconducting ferromagnetic materials becomes essential for developing novel metal–organic frameworks that exhibit spintronic phenomena [19–25]. Here, the correlation between these two phenomena can be examined by the proper choice of multi-dentate and the metal centers (type, oxidation state, etc.) [26–29]. The role of π–conjugated coordinating ligands known as spacers to facilitate charge carriers transport (electron/hole), energy transfer and mediate spin delocalization through super-exchange mechanism between similar ($M\text{-}L_2\text{-}M$) and dissimilar ($M\text{-}L_2\text{-}M'$) paramagnetic metal sites is attracting increasing interest [19–25]. In particular, the incorporation of paramagnetic metal centers into delocalized π–conjugated organic systems can modulate energy states of the π–system by matching the HOMO–LUMO energy levels of the spacer with redox levels of the metal sites [28]. This energy state modulation affords novel materials with diverse electro-, photo- and magneto properties. In this context, photo-magnetism, and its relevance to spin-current, energy transfer, and energy inter-conversion have been in the focus of several interesting academic and technological investigations including solar energy (PV), photocatalysis, sensors, light emitting diode (LED) and others [1, 5, 9–13, 30].

To date, the most studied ditopic ligands rely on the use of pyridine-based (bi, ter- and oligo-pyridine), imine,

✉ Isam M. Arafa
isamaraf@just.edu.jo

[1] Department of Applied Chemistry, Faculty of Science and Arts, Jordan University of Science and Technology, P.O. Box 3030, Irbid 22110, Jordan

aza-heterocyclic, dicarboxylate, 8-hydroxyquinoline and other multidentate functionalities [2, 9, 11, 26–29]. However, oxime-based ditopic ligands are infrequently addressed [31–34]. In this study, we present a ditopic imine-oxime ligand (**H_2L**) where the imine-oxime functionalities are separated by an aromatic phenylene spacer, Fig. 1. The present system is designed in such a way to allow the magnetic sites incorporated within the backbone to interact via π–conjugated mediator (spacer) having luminescence capabilities. The backbone of the desired BMCs is composed of extended π-conjugated molecular arrays of $\mathbf{L^{2-}}$ ligand connecting similar [Cu^{II}-L_2-Cu^{II}], [Ni^{II}-L_2-Ni^{II}], [$ClFe^{III}$-L_2-$Fe^{III}Cl$], and dissimilar [Cu^{II}-L_2-$Fe^{III}Cl$], and [Ni^{II}-L_2-$Fe^{III}Cl$] BMCs. The latter dissimilar two chloro complexes were further used to generate μ-oxo-[Cu^{II}-L_2-Fe^{III}], and μ-oxo-[Ni^{II}-L_2-Fe^{III}] BMCs. In this system, the metal sites constitute a crucial part of the structural backbone where the isolated metal centers are weakly interacting via the π-spacer. The obtained ditopic ligand and the corresponding BMCs are characterized by spectroscopic (Uv–Vis, FT-IR, ^{1}H-NMR), mass spectrometric (MS), powder X-ray diffraction (P-XRD) and scanning electron microscopic (SEM) techniques. The ability of this imine-oxime spacer to mediate charge transfer and spin–spin exchange between the metal sites are examined by investigating their solid-state DC electrical conductivity and static magnetic susceptibility/moment characteristics. A magnetic thin film composed of the μ-oxo-[Ni^{II}-L_2-Fe^{III}] in polymethamethylacrylate matrix is produced using solvent casting method and its magnetic and photochromic properties are qualitatively displayed. The incorporation of molecular/macromolecular magnetic species into elastic polymeric system offers a crucial step for the advancements of magnetoelastic membranes/ thin films. Such stimulus responsive magnetic smart materials pave the road to applications in different applied sciences and technology.

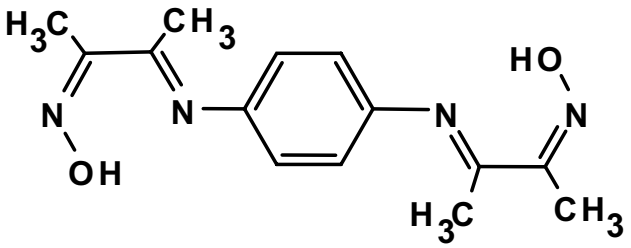

Fig. 1 Schematic structure of the imino-oxime ditopic ligand (H_2L)

2 Materials and Methods

All chemicals and solvents were reagent grade and used as received (triethylamine, Scharlau; 1,4-phenylenediamine, Ferak-Berlin, GmbH; 2,3-Butanedionemonoxime, Janssen Chimica; anhydrous $FeCl_3$, CHEMEX; $CuCl_2.2H_2O$, M&B; $NiCl_2.6H_2O$, M&B). Elemental analysis (C, N, H) were performed using Euro-EA elemental analyzer. The lattice water of crystallization was determined using a Sartorius thermo-balance at 120 °C. UV–visible spectra were recorded on a Shimadzu double beam UV–Vis spectrophotometer UV-2550. FT-IR spectra were recorded on a Nicolit Impact 410 FT-IR spectrophotometer (4000-400 cm^{-1}, KBr pellets). ^{1}H-NMR spectra were recorded on a Bruker 400 MHz instrument in $CDCl_3$. Powder X-ray diffraction (P-XRD) was performed on a Philips X-ray spectrometer (PW 1729, $K_{\alpha l}$ of Co source, λ = 1.789 Å, 35 kV, 40 mA, 2 θ = 6–100°). The textural morphology was investigated on a SEM-FEI Philips microscope (sputter-coated with gold, Polaron E6100, 1200, 20 kV). Mass spectral studies were done by ESI-MS on Agilent Corporation Applied Biosystems, USA (API 3200 LC/MS/MS system, triple quadrapole detector, Mass-Hunter workstation software). Ionization was achieved electrospray ionization (acetonitrile/water) technique operating in turbo-spray mode under negative mode in the case of the H_2L ligand but under positive ion mode conditions in the case of the BMCs. The current–voltage (I-V) characteristics were performed on compressed circular discs (7 ton/cm^2, 5 min, radius = 6.51 mm, thickness 400–600 μm) of 0.10–0.20 g of dry fine powder, sandwiched between two polished brass electrodes. The current passing through the sample was measured using metravo electrometer (± 0.1 nA) as a function of potential difference (0–120 V) using Fluke and Philips digital multimeter. Magnetic susceptibility measurements were carried out using a Sherwood static magnetic susceptibility balance at room temperature.

2.1 *Synthesis of the 1,4-Phenylene-bis(2,3-butanedeimineoxime) Ditopic Ligand (H_2L)*

1,4-phenylenediamine (5.41 g, 50 mmol, recrystallized from benzene) was mixed with 2,3-butanedionemonoxime (10.10 g, 100 mmol) in 50 mL absolute ethanol. The reaction mixture was heated in a water bath (70 °C, 30–60 min) after which the solvent was removed under reduced pressure in a rotary-evaporator. The dark yellow powder was collected, dried under vacuum (70 °C, 2–3 h.) and stored in a closed container for further use. **$H_2L{\cdot}H_2O$**: Yield: 10.8 g (~ 70%). Color/state: dark yellow powder. M.

Pt: 172–174 ºC. Elemental analysis for [$C_{14}N_4O_2H_{18}{\cdot}H_2O$]: found (calculated) %: C, 57.21 (57.53); N, 18.19 (19.18); H, 6.89 (6.85). MS (m/z, relative intensity, assignment): 273,100%, [H_2L–H]; 256, 20%, [H_2L–H_2O]. ^{1}H-NMR ($CDCl_3$, δ ppm): 1.69 (t, 6H, imine CH_3), 2.21 (t, 6H, oxime CH_3), 3.97 (br, 2H, oxime), and 6.60–6.75 (m, 4H, Ar–H).

2.2 *Formation of the Homobimetallic [Cu^{II}-L_2-Cu^{II}], [Ni^{II}-L_2-Ni^{II}] and [$ClFe^{III}$-L_2-$Fe^{III}Cl$] BMCs*

A solution of 0.01 mol of the corresponding metal salts (1.62 g, $FeCl_3$; 1.71 g, $CuCl_2.2H_2O$; 2.38 g, $NiCl_2.6H_2O$) dissolved in 25 mL ethanol was added to a solution of the H_2L ligand (2.74 g, 0.01 mol) dissolved in 25 mL ethanol kept in a round bottom flask. The reaction mixture is then subjected to sonication for about 6 h. during which excess triethylamine (6.0 mL) base was added. The solvent was removed under reduced pressure and the product was isolated, washed with aqueous ethanol (20%), filtered off, vacuum dried (70 °C), and stored under vacuum for further use.

[Cu^{II}-L_2-Cu^{II}]·4H_2O: Yield: ~ 48%; Color/state: dark brown powders; M. Pt: 146–148 ºC.

[Ni^{II}-L_2-Ni^{II}]·3H_2O: Yield: ~ 83%; Color/state: brown powder; M. Pt: 251–289 ºC decom.

[$ClFe^{III}$-L_2-$Fe^{III}Cl$]·6H_2O: Yield: ~ 91%; Color/state: dark brown powder; M. Pt:152–155 ºC.

2.3 *Formation of the Heterobimetallic [Cu^{II}-L_2-$Fe^{III}Cl$] and [Ni^{II}-L_2-$Fe^{III}Cl$] BMCs*

This macromolecular complex was constructed through a multi-step in situ procedure as shown in Scheme 1. In step **I**, 1,4-phenylenediamine (0.54 g, 5.0 mmol) was reacted with 2,3-butanedionemonoxime (0.51 g, 5.0 mmol) in 50 mL ethanol (70 ºC, ~ 30 min.) to form the first half of the imine-oxime ligand. To this reaction product, the divalent metal is introduced ($CuCl_2.2H_2O$, 0.86 g, 5.0 mmol; $NiCl_2.6H_2O$, 1.19 g, 5.0 mmol) followed by addition of triethylamine (1.0 mL) as given in step **II**. The reaction was sonicated for ~ 1 h. to ensure complexation. This step is followed by the addition of 2,3-butanedionemonoxime (0.51 g, 5.0 mmol) in which the second part of the ditopic imine-oxime ligand is attached, as shown in step **III**. Here, the reaction mixture was sonicated (70 ºC, ~ 30 min.) followed by the addition of anhydrous $FeCl_3$ (0.81 g, 5 mmol) and triethylamine (1.0 mL). The reaction mixture was further subjected to sonication for 3–4 h. at 60–70 ºC, step **IV**. The final product was precipitated by partial removal of ethanol under reduced pressure, filtered, and washed with aqueous ethanol (20%) to remove the $Et_3N{\cdot}HCl$ salt. The resulting powder was dried

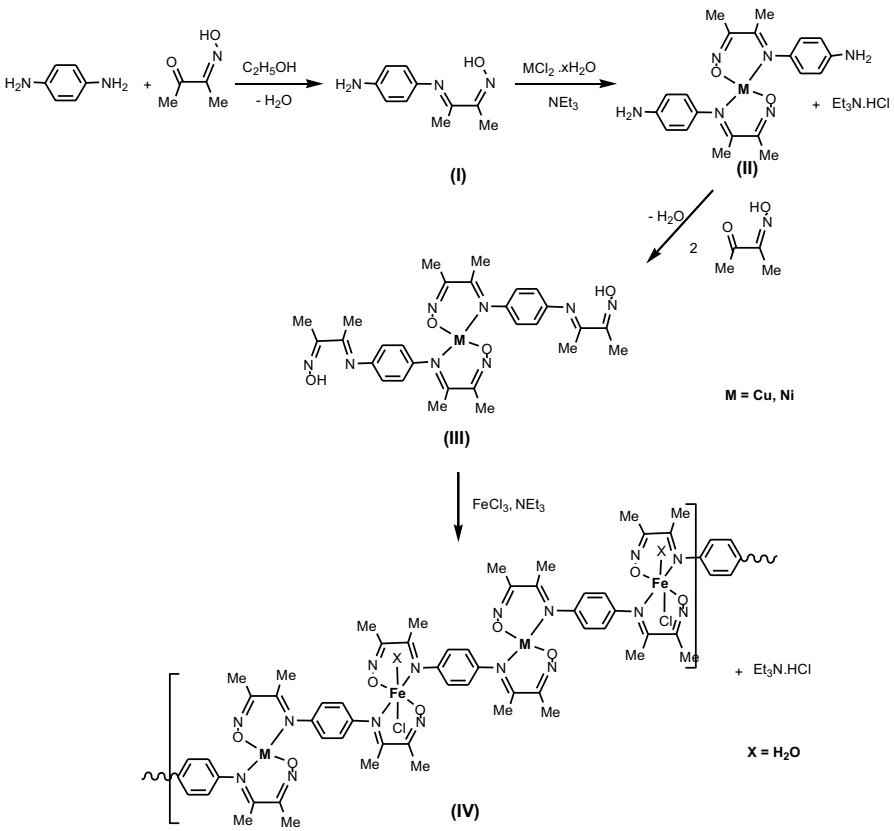

Scheme 1 A reaction scheme depicting the in situ multi-step procedure used to construct [M^{II}-L_2-$Fe^{III}Cl$] heterometallic BMCs (M^{II} = Cu^{II}, Ni^{II})

under vacuum (70 ºC, 3–4 h.) and stored in a closed container for further use.

[Cu^{II}-L_2-$Fe^{III}Cl$]0.5H_2O: Yield: ~ 78%; Color/state: dark brown powder; M. Pt: 118–120 ºC.

[Ni^{II}-L_2-$Fe^{III}Cl$]0.4H_2O: Yield: ~ 50%; Color/state: dark brown powder; M. Pt: > 350 ºC.

2.4 *Formation of the μ-oxo-[Cu^{II}-L_2-Fe^{III}] and μ-oxo [Ni^{II}-L_2-Fe^{III}] BMCs*

1.00 g of the corresponding bimetallic [Cu^{II}-L_2-$Fe^{III}Cl$] and [Ni^{II}-L_2-$Fe^{III}Cl$] BMCs was added to a 10% ethanolic solution of NaOH (pH = 8) at ambient conditions, Scheme 2. The reaction mixture was sonicated for 3hrs. The products were isolated as described earlier.

μ-oxo-[Cu^{II}-L_2-Fe^{III}]0.4H_2O: Yield: ~ 82%; Color/state: black powder; M. Pt: > 350 ºC.

μ-oxo-[Ni^{II}-L_2-Fe^{III}]0.4H_2O: Yield: ~ 93%; Color/state: brown powder; M. Pt: > 350 ºC.

2.5 Formation of Magnetic Thin Films

The obtained μ-oxo-[Ni^{II}-L_2-Fe^{III}] BMCs (0.25 g) was suspended in about 3–5 mL of DMSO/THF (1:1 mixture vol/vol) containing polymethylmethacrylate (0.50 g, PMMA). The suspension was subjected to sonication (~ 70 °C, 2–3 h.) to form a colloidal solution, which then casted on clean glass plates, dried and aged (1–2 days, ~ 70 °C). The deposited films were smoothly peeled off to finally afford translucent-opaque microscopic films of ~ 100 μm in thickness.

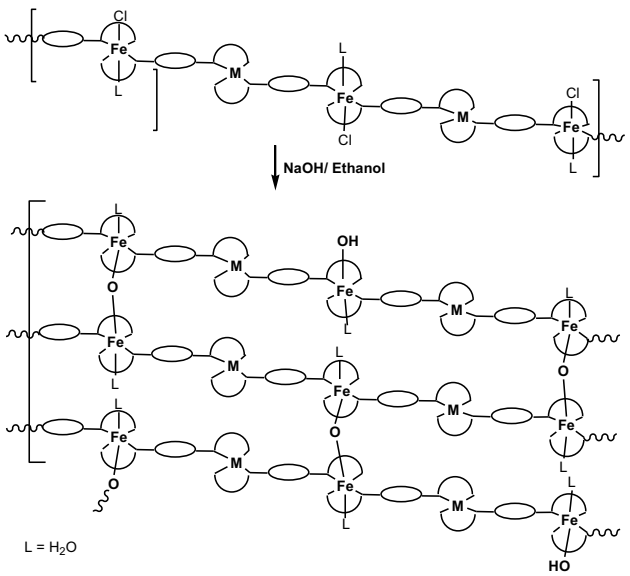

Scheme 2 A reaction scheme depicting the formation of μ-oxo[M^{II}-L_2-Fe^{III}] Extended BMCs (X = H_2O; M^{II} = Ni^{II}, Cu^{II})

3 Results and Discussion

3.1 Synthesis of BMCs

Schemes 1, 2 depict the synthetic strategies employed for the preparation of the desired heterobimetallic [M^{II}-L_2-$Fe^{III}Cl$] BMCs and their conversion into the corresponding μ-oxo-[M^{II}-L_2-Fe^{III}] macro complexes (M^{II} = Cu^{II}, Ni^{II}). To ensure a high level of metal distribution is achieved, a four-step *in-situ* procedure was employed under continuous sonication [24]. This four-step procedure is shortened in one-step method in the case of the homometallic [Cu^{II}-L_2-Cu^{II}], [Ni^{II}-L_2-Ni^{II}], and [$ClFe^{III}$-L_2-$Fe^{III}Cl$] BMCs. The obtained BMCs are soluble in polar organic solvents such as CH_3CN, DMSO but partially soluble in CH_2Cl_2. The introduced μ-oxo bridges permit chain-chain cross-linking at the Fe^{III} sites allowing the generation of new structural arrays of ladder-like macro-conformation and ultimately unique morphology (vide infra). The formation of the BMCs is clearly suggested by the mass spectral data where the molecular ion fragments due to [M^{II}-L_2-$Fe^{III}Cl$)] and μ-oxo-[M^{II}-L_2-Fe^{III}] are observed. Inspection of observed m/z values and the calculated molecular mass are consistent with the assigned structure. The low intensity fragment clusters appearing at high m/z values clearly indicate the existence of dimers and trimmers. Unfortunately, no conclusion can be drawn from the MS data concerning the degree of oligomerization because the macromolecular complexes may undergo degradation during the electrospray ionization process.

3.2 Electronic Spectroscopy

The electronic absorption spectral data of the prepared ditopic ligand (H_2L) and all the BMCs are listed in Table 1 and displayed in Fig. 2. The UV–Vis. spectrum of H_2L displays two unresolved UV bands at 253 and 274 nm assigned to π-π*and n-π* transitions with a minor low-energy tail in 340–420 nm range. These UV transitions split and undergo observable shift upon coordination in [Cu^{II}-L_2-Cu^{II}], [$ClFe^{III}$-L_2-$Fe^{III}Cl$] and [Ni^{II}-L_2-$Fe^{III}Cl$] BMCs. However, the shape of these two bands undergo minor changes in [Ni^{II}-L_2-Ni^{II}] but becomes broad in [Cu^{II}-L_2-$Fe^{III}Cl$]. Interestingly, these two intense bands merge in one band at 253–260 nm in the μ-oxo-[M^{II}-L_2-Fe^{III}] of both the Cu^{II} and Ni^{II} BMCs. Furthermore, the molar absorptivity of the free ligand is typical for π-system ($\varepsilon \approx 8.9 * 10^4\ M^{-1}\ cm^{-1}$) which upon coordinating the metal ions undergo low-moderate decrease to reach a value of $\varepsilon \approx 1.3–5.9 * 10^4$. This observation implies that this UV band is mainly due to π-π* transition.

Table 1 UV–Vis and FT-IR spectral data of the prepared H_2L, homo- and hetero-bimetallic macromolecular complexes (BMCs)

Bimetallic macromolecular complexes	λ (nm) [a]	ν (cm^{-1})[b]				
		υ_{O-H}	υ_{C-H}	$\upsilon_{C=NOH}$	$\upsilon_{C=NAr}$	υN-O
H_2L	254; 275*; 340_{sh}	3382; 3300; 3213	3021; 2820	1684;	1624	966; 885
[Cu^{II}-L_2-Cu^{II}]	271*; 400**	3378	3037; 2978	1600	1512	877; 830
[Ni^{II}-L_2-Ni^{II}]	284*; 320**	3372	2954; 2923	1606	1503	993; 854
[$ClFe^{III}$-L_2-$Fe^{III}Cl$]	271*; 302; 560**	3351	2938; 2746	1619	1512	1002; 826
[Cu^{II}-L_2-$Fe^{III}Cl$]	271*; 300; 524**	3357; 3201	2981; 2938	1603	1503	973; 940
[Ni^{II}-L_2-$Fe^{III}Cl$]	289*; 520**	3357; 3201	3034; 2984	1618	1572	995; 850
μ-oxo-[Cu^{II}-L_2-Fe^{III}]	253*; 385**	3415	2968; 2930	1566	1551	926;870
μ-oxo-[Ni^{II}-L_2-Fe^{III}]	260*; 340_{sh}; 380**	3435	2960; 2927	1588	1455	926; 860

[a]The H_2L in $CHCl_3$ ($\varepsilon \approx 8.9 * 10^4\ M^{-1}\ cm^{-1}$); * refers to π-π*/n-π*transition bands ($\varepsilon \approx 1.3–5.9 * 10^4$), ** refers to LMCT band ($\varepsilon \approx 2.1–4.1 * 10^3\ M^{-1}\ cm^{-1}$) of BMCs in DMSO

[b]KBr pellets

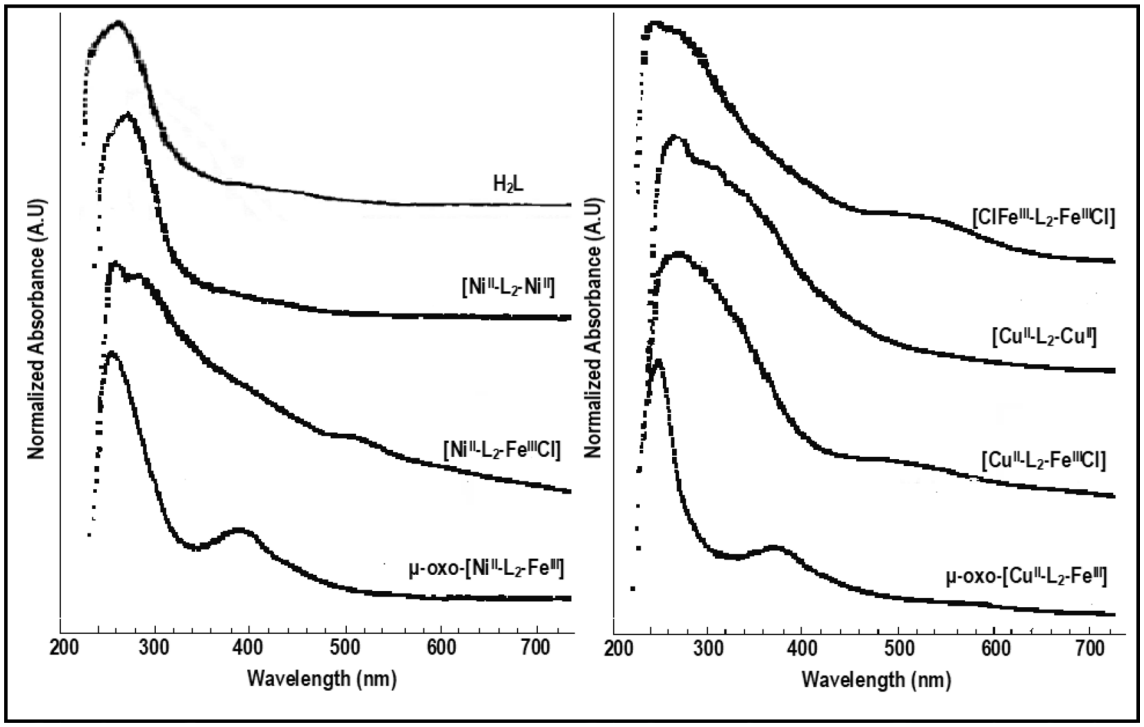

Fig. 2 UV–Vis. absorption spectra of the prepared H_2L ligand, and the corresponding homo- and hetero-bimetallic BMCs

Moreover, the prepared μ–oxo-[M^{II}-L_2-Fe^{III}] BMCs exhibit well-defined visible band due LMCT band (ligand-to-metal charge transfer) of moderate intensity ($\varepsilon \approx 2.1–4.1 * 10^3\ M^{-1}\ cm^{-1}$) in the visible region at 380–385 nm. This type of transition (LMCT) red-shifted to 520–560 nm region in the bimetallic BMCs containing Fe^{III} centers but appears as shoulders at 320–400 nm region in the case of the bimetallic [Ni^{II}-L_2-Ni^{II}] and [Cu^{II}-L_2-Cu^{II}] BMCs. Here, the intense transitions due to π-π*/n-π* and LMCT bands obscure the observation of d-d transitions, Fig. 2.

3.3 FT-IR Spectroscopy

The formation of these BMCs is also supported by the FT-IR spectral data. Figure 3 depicts the FT-IR spectra of the prepared binuclear ligand (H_2L), and corresponding homo- and hetero-bimetallic BMCs recorded in the region 4000-400 cm^{-1} as KBr pellets. Characteristic FT-IR frequencies and their assignments are presented in Table 1. The stretching frequencies of imine ($\nu_{C=N}$), and oxime, ($\nu_{C=NO;}$ ν_{N-O}) functionalities are of particular importance in the structural elucidation of the imine-oxime backbone in the prepared

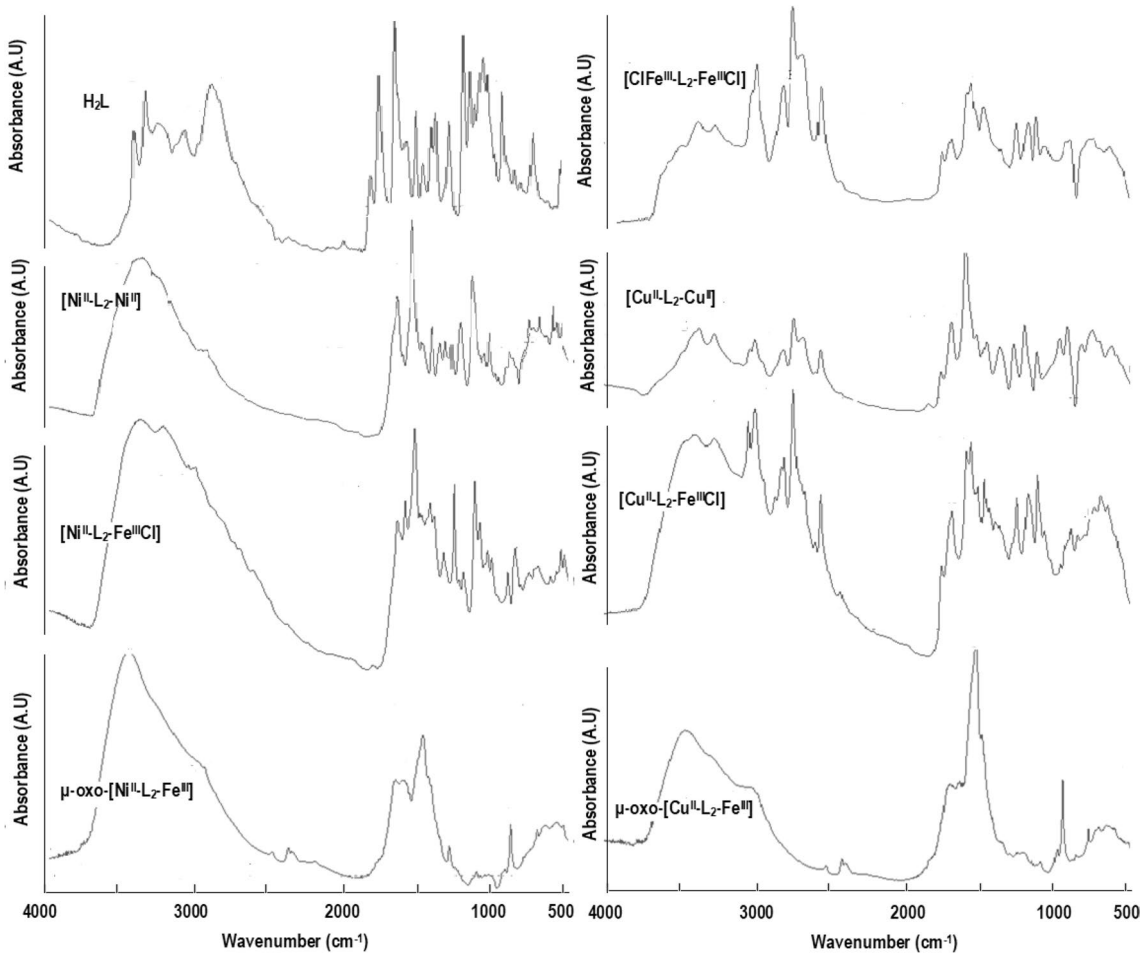

Fig. 3 FT-IR spectra of the prepared H_2L ligand and the corresponding BMCs

ditopic H_2L ligand and the corresponding homo- and hetero-BMCs [31–34]. The observed broad bands in the spectra at 3400-3200 cm^{-1} region can be conveniently assigned to the stretching frequency ($\nu_{O\text{-}H}$) of the coordinated and lattice water. The bands in the 1600-1500 cm^{-1} regions are attributed to the imine ($\nu_{C=N}$) and oxime/oximate ($\nu_{C=NO}$) stretching frequencies. Inspection of the effect of Cu^{II}, Ni^{II} and Fe^{III} coordination on these frequencies shows that the imine bands are shifted to lower values by 52–121 cm^{-1} while the oxime band shifts by 65–84 cm^{-1}. These shifts are more pronounced in the μ-oxo bridged species (μ-oxo-[M^{II}-L_2-Fe^{III}]) where they become 73–169 cm^{-1} and 96–118 cm^{-1}, respectively. This substantial shift clearly indicates strong attachment of the metal centers to the imine-oxime chelating moieties. Close examination of these peaks shows that the oximate peak ($\nu_{C=NO}$) appears as a relatively broad or split peak which reflects distorted octahedral geometries at the metal centers due to mixed imine-oxime/di-imine ligations shown in Fig. 4. The broadening/ splitting behavior of the $\nu_{C=N}$ band is also observed but to a lower extent than

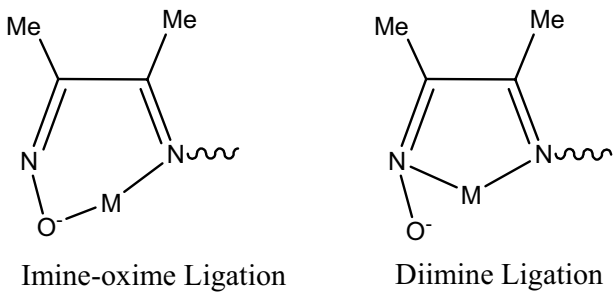

Fig. 4 Expected ligation in imine-oxime complexes

those of $\nu_{C=NO}$. This observation can be explained based-on the fact that the imine groups are engaged in the extended π-conjugation with the phenylene spacer imparting low skeletal flexibility. Indeed, this conclusion on the rigidity of the skeletal structure is further supported by the bulk melting points of these complexes where the μ-oxo-[M^{II}-L_2-Fe^{III}] BMCs exhibit high melting/decomposition temperatures

(> 350 ºC). In fact, the observed structural rigidity should have its own implication on the electrical and magnetic properties of μ-oxo-bridge species, vide infra. Furthermore, the FT-IR spectral data of H_2L shows a strong peak at 966 cm^{-1} and weak peak at 885 cm^{-1}assigned to $\nu_{N\text{-}O}$. A close look at the position of the first peak in the BMCs shows shits to higher frequencies (973–1002 cm^{-1}) in homo- and hetero- BMCs except the μ-oxo-[M^{II}-L_2-Fe^{III}] where it shifts to 926 cm^{-1}.

3.4 Powder X-ray Diffraction (P-XRD)

Figure 5 depicts the P-XRD profiles of the H_2L ditopic ligand, the corresponding homo- and hetero-bimetallic BMCs. The diffraction peaks, interchain spacing distance, crystallite size, and crystallinity percentage are summarized in Table 2. Inspection of the P-XRD profile and diffraction data of the H_2L ligand shows that it displays multiple sharp diffraction peaks superimposed on a broad amorphous feature centered at 2θ of 24.4°. The low crystallinity ratio of about 23% as estimated from the area under the peaks reflects the vitreous nature of the ligand system. Furthermore, the estimated interchain spacing distance of 4.2 Å as determined from Braggs Function (**$n\lambda = 2d \sin \theta$**) demonstrates that the ditopic ligands are held together by nonspecific weak intermolecular interactions ascribed to H-bonding of the oxime end groups and π-π stacking of the phenylene spacer in agreement with the its low melting point (172–174 ºC). The crystallite size as estimated from Scherrer`s Formula (**$L = K\,\lambda/\beta\cos\theta$**) where L, K, λ, β and θ are crystallite size, Scherrer constant, wavelength of X-Ray beam, width at half-height in radian, and diffraction angle, respectively) was relatively small (4.3 Å).

General comparison between the P-XRD patterns of the H_2L ligand with those of the BMCs shows that the presence of metal ions resulted in dramatic change in their structures.

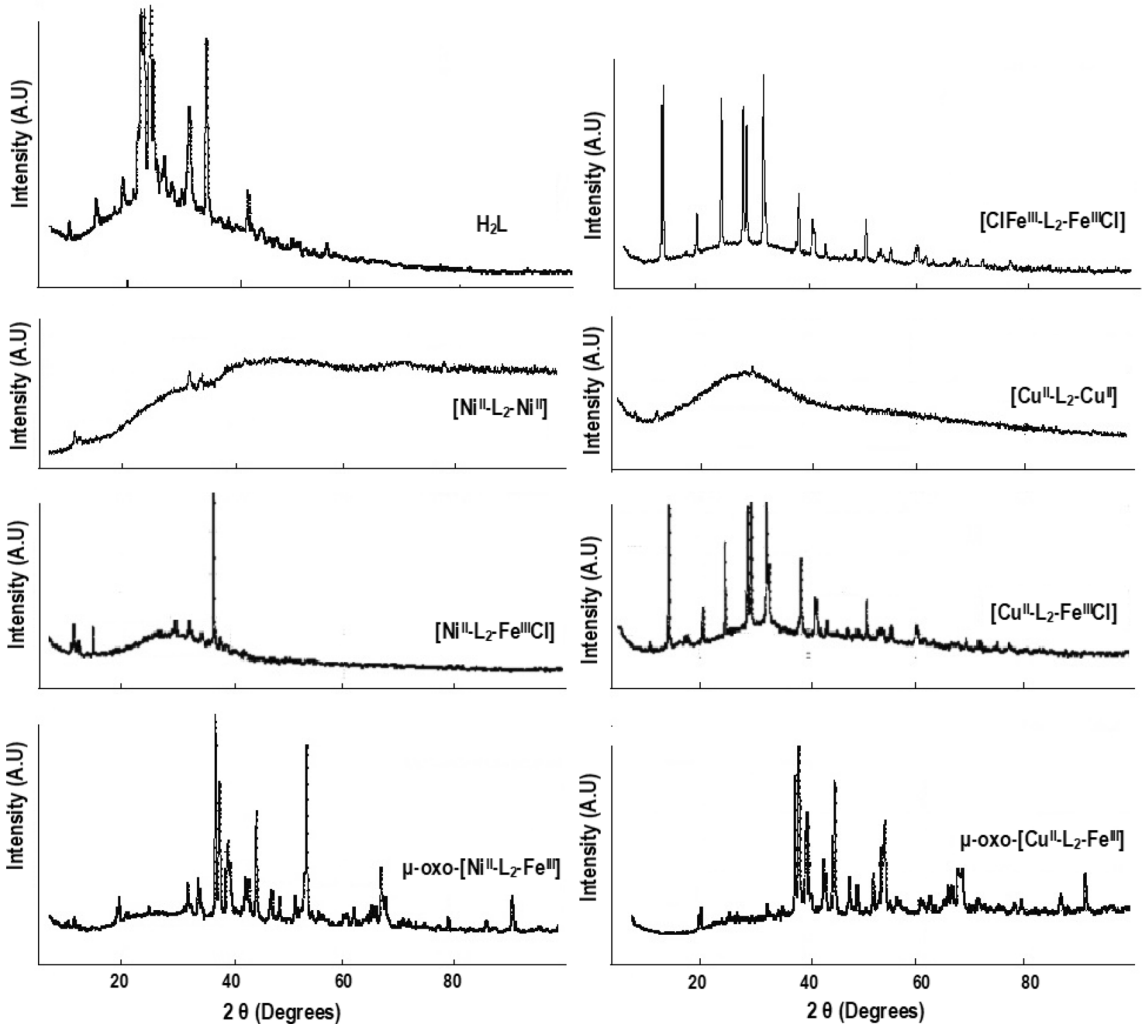

Fig. 5 P-XRD diffraction profiles prepared H_2L ligand and the corresponding BMCs

Table 2 Characteristic P-XRD peaks, chain-chain d-spacing, crystallite size and crystallinity of the obtained imine-oxime ligand (H_2L), and the investigated binuclear BMCs

Bimetallic macromolecular complexes	2θ (degrees)[a]	Interchain spacing[b] (Å)	Crystallite Size[c] (Å)	Crystallinity (%)[d]
H_2L	9.5, 14.7, 19.5, **24.4***, 28.3, 29.4, 33.7, 41.4	4.2	4.3	23
[Cu^{II}-L_2-Cu^{II}]	8.2, **28.4*,** 29.9, 34.2, **53.2**	3.6	5.1	Negligible
[Ni^{II}-L_2-Ni^{II}]	12.0, **26.6,** 32.6, 34.8, **46.7*, 71.0,** 78.5	3.2	4.4	~5
[ClFe^{III}-L_2-Fe^{III}Cl]	14.6, 20.6, 25.1, **29.0*,** 29.3, 30.6, 51.0, 60.1	3.6	5.3	51
[Cu^{II}-L_2-Fe^{III}Cl]	14.6, 20.8, 25.3, **31.8*,** 38.8, 41.4, 50.2, 51.2	3.3	4.5	42
[Ni^{II}-L_2-Fe^{III}Cl]	11.3,15.5, **30.0***, 30.2, 32.2, 34.6, 36.8	3.5	3.7	38
μ-oxo-[Cu^{II}-L_2-Fe^{III}]	20.2, 37.9, 38.1, 39.5, **41.3*,** 43.7, 44.8, 47.5, 49.2, 52.1, 67.1**,** 91.1	2.5	6.7	58
μ-oxo-[Ni^{II}-L_2-Fe^{III}]	19.7, 32.2, **32.4**, 34.6, 37.9, 38.6, **42.7***, 44.8, 47.2, 48.8, 51.7, 67.2, 90.7	2.4	9.1	47

[a]The bold values refer to the broad diffraction peak

[b]Chain-chain distance (d-spacing) is calculated of the broad peak indicated with * using Braggs' Law (nλ = 2d sin θ), n = order of diffraction, λ (Å) is the wavelength of the X-ray beam, θ is the diffraction angle

[c]Crystallite size is calculated from Scherrer's Formula (L = K λ/βcosθ) where L (crystallite size), K (Scherrer constant), λ (wavelength of X-Ray beam), β (width at half-height in radian) and θ (diffraction angle)

[d]% crystallinity is estimated from the ratio of the area under the sharp peaks to total area under the diffraction profile

Interestingly, the P-XRD profiles of [Cu^{II}-L_2-Cu^{II}] and [Ni^{II}-L_2-Ni^{II}] exhibit high amorphous structures unlike the other BMCs which exhibit the coexistence of sharp crystalline peaks superimposed on broad amorphous diffraction profile. This structural alteration is associated with moderate reduction of the interchain spacing distance by ~ 0.6–1.0 Å in homo- and hetero- BMCs except μ-oxo-[M^{II}-L_2-Fe^{III}] species where substantial interchain spacing reduction from 4.2 Å in H_2L to 2.4–2.5 Å is observed. These observations are indicative of an increase in the overall structural compactness of the crystal lattice especially in the μ-oxo-[M^{II}-L_2-Fe^{III}] species, Table 2.

A close look at the diffraction data of the μ-oxo-[M^{II}-L_2-Fe^{III}] complexes and their chloro precursors [M^{II}-L_2-Fe^{III}Cl] shows that the interchain separation distances undergo further decrease of ~ 0.9–1.0 Å upon the formation of the μ-oxo-bridge. This change in the interchain distances is also accompanied by an increase in crystallinity with different increase in the crystallite size as seen in the corresponding Cu^{II} (from 4.5-to-6.7 Å) and Ni^{II} (from 3.7-to-9.1 Å) species.

3.5 Textural Morphology

The obtained SEM micrograph images in Fig. 6 show that the prepared macromolecular systems possess different textural morphologies. The SEM image of H_2L ligand displays interconnected macromolecular architecture with different cavity shape and size (1–7 μm). The interconnected porous morphology with channeling features suggests that these materials can be thought of as potential candidates for gas storage [2, 6, 7]. Furthermore, the observed diffused boundaries are in accordance with the vitreous nature seen in the P-XRD of this ditopic ligand.

On the other hand, the homo-bimetallic of [Ni^{II}-L_2-Ni^{II}] forms a cracked layer made of connected tiny particles (0.8–3.6 μm) of irregular shape forming super lattice structure. However, two SEM images are provided for the [Cu^{II}-L_2-Cu^{II}] analog identified as **A** which refers to the complex as isolated while **B** shows the texture after heat treatment to ~ 160 °C. In both cases, the particles adopt globular structure of ~ 500 nm in size before heat treatment which upon heat treatment retains its globular nature but becomes enlarged (500–1500 nm) and interconnected by a soft structure. This property is typical for polymeric structures. Unlike these two homo-bimetallic, the [ClFe^{III}-L_2-Fe^{III}Cl] forms randomly oriented rod-like structure of irregular shape and size (2.5 × 12 μm).

However, the hetero-bimetallic [Cu^{II}-L_2-Fe^{III}Cl] adopts rod-like structure (4.5 × 15 μm) while its μ-oxo-[Cu^{II}-L_2-Fe^{III}] adopts loose micro particles textures of irregular shape (~ 2.5 μm) associated with tiny rod-like texture of 0.8 × 7.5 μm dimension. Amazingly, the textural morphology of the μ-oxo-[Ni^{II}-L_2-Fe^{III}] and its [Ni^{II}-L_2-Fe^{III}Cl] chloro precursor while the precursor adopt nano-scale globular texture (150–400 nm) the μ-oxo-[Ni^{II}-L_2-Fe^{III}] adopts relatively long needle-like rods (0.1 × 30–50 μm) morphology. Interestingly, the nano-rods are self-arranged in a highly ordered fashion parallel to each other.

The dramatic transformation in the texture can be understood by considering the interchain forces where the non-specific H-bonding and π-π stack interactions that exist in

the free ligand are replaced by different electrostatic/coordinate bonds in the homo- and hetero BMCs. The presence of an axial Cl, H_2O, OH or μ-oxo-bridge enhances the possibility of the particles to further self-assemble and fold to generate globular texture as in the case of [Ni^{II}-L_2-$Fe^{III}Cl$] or twist to afford low-dimensional helical arrays that appear as rod-like textures as seen in the case of μ-oxo-[Ni^{II}-L_2-Fe^{III}]. In fact, helical and rod-like textures are reported in several metal-containing organic frameworks [26–28].

3.6 Magnetic Characteristics of the Prepared of the Homo- and Hetero-bimetallic Macro-complexes (BMCs)

The magnetic behavior of the prepared homo- and hetero-bimetallic BMCs was investigated using a static magnetic susceptibility method at room temperature. The obtained magnetic data is summarized in Table 3. The obtained effective magnetic moment values ($\boldsymbol{\mu_{eff}}$) are compared with the corresponding spin magnetic moment for magnetically non-interacting metal ion pairs [M-L_2-M`] using the isolated spin states additive rule as given in Eq. 1. where $\mu_{spin(M)} = g[S(S+1)]^{1/2}$, S and g are the total spin of each of the magnetic site and the gyromagnetic ratio (2.0023), respectively. The $\boldsymbol{\mu_{eff}}$ values are compared to the corresponding $\boldsymbol{\mu_{spin\ (M\text{-}L2\text{-}M`)}}$ to deduce the type of M-M` magnetic interaction / coupling across the π-spacer and μ-oxo bridge.

$$\boldsymbol{\mu spin(M-L2-M\})} = \boldsymbol{\mu spin(M)} + \boldsymbol{\mu spin(M\})} \quad (1)$$

The magnetic data in Table 3 show three interesting observations for the homo- BMCs of [Cu^{II}-L_2-Cu^{II}], [Ni^{II}-L_2-Ni^{II}], and [$ClFe^{III}$-L_2-$Fe^{III}Cl$]. First, the **[Cu^{II}-L_2-Cu^{II}]** exhibits low μ_{eff} of 1.98 BM relatve to the value expected from pure spin state of 3.46 BM, thus resulting in substantial magnetic quenching (-1.48 BM) leading to strong antiferromagnetic coupling. Second, the observed μ_{eff} of 5.14 BM for the **[Ni^{II}-L_2-Ni^{II}]** pair reveals that the Ni^{II} metal ions adapt distorted octahedral (O_h) geometries (d^8, $t_{2g}{}^6e_g{}^2$) rather than the diamagnetic square planar geometry (d^8, $t_{2g}{}^6d_{z2}{}^2$). The observed magnetic quenching of (- 0.52 BM) suggests moderate antiferromagnetic interaction between the magnetic sites. Third, the observed magnetic response for the **[$ClFe^{III}$-L_2-$Fe^{III}Cl$]** pair of $\boldsymbol{\mu_{eff}} = 3.29$ BM is unexpectedly low demonstrating that the Fe^{III} metal centers adapt low spin state (LS, d^5, $t_{2g}{}^5$, S = ½, $\mu_{spin} = 1.73$ BM) in a distorted octahedral (O_h) geometry rather than the high spin states (HS, d^5, $t_{2g}{}^3e_g{}^2$, S = 5/2, $\mu_{spin} = 5.92$ BM). This implies that the Fe^{III} is strongly bound to the ditopic ligand causing large crystal field splitting. Nevertheless, the low

Table 3 Gram magnetic susceptibility (χ_g), effective magnetic moment (μ_{eff}), calculated spin magnetic moment ($\boldsymbol{\mu_{spin\ (M\text{-}L2\text{-}M`)}}$), and M-M` magnetic interaction of the investigated binuclear BMCs

BMCs	χ_g (10^6) (emu)	M. Mass g/mole	μ_{eff}[a] (BM)	$\mu_{spin\ (M\text{-}L2\text{-}M`)}$[b] (BM)	$\Delta\mu = \mu_{eff} - \mu_{spin}$[c] (BM)	M-M` Magnetic interaction[d]
[Cu^{II}-L_2-Cu^{II}]	2.2	743.0	1.98	3.46	− 1.48 Mag. Quenching	Antiferromagnetic [Cu^{II}-Cu^{II}]
[Ni^{II}-L_2-Ni^{II}]	16.6	661.4	5.14	5.66	− 0.52 Mag. Quenching	Antiferromagnetic [O_h Ni^{II}-O_h Ni^{II}]
[$ClFe^{III}$-L_2-$Fe^{III}Cl$]	5.4	834.6	3.29	3.46	− 0.17 Mag. Quenching	Antiferromagnetic [LS Fe^{III}-LS Fe^{III}]
[Cu^{II}-L_2-$Fe^{III}Cl$]	4.5	788.8	2.92	3.46	− 0.54 Mag. Quenching	Antiferromagnetic [Cu^{II}-LS Fe^{III}]
[Ni^{II}-L_2-$Fe^{III}Cl$]	17.8	766.0	5.72	4.56	+ 1.16 Mag. Enhancement,	Ferromagnetic [$O_h Ni^{II}$-LS Fe^{III}]
μ-O-[Cu^{II}-L_2-Fe^{III}]	91.7	751.3	12.87	11.84	+ 1.03 Mag. Enhancement	Ferromagnetic [HS Fe^{III}-**O**-HS Fe^{III}]
μ-O-[Ni^{II}-L_2-Fe^{III}]	83.3	746.5	12.23	11.84	+ 0.39 Mag. Enhancement	Ferromagnetic [HS Fe^{III}-**O**-HS Fe^{III}]

[a] $\boldsymbol{\mu_{eff}} = 2.83\ (\chi_m \times T)^{1/2}$, χ_m is the molar magnetic susceptibility per binuclear complex [M-**L_2**-M`] at room temperature (300 K). $\chi_m = \chi_g \times$ M.Wt; Experimental literature values for single metal centers, d^9 $Cu^{II} = 1.7–2.2$ BM; d^8 $Ni^{II} = 2.9–3.3$ BM; d^5 ($t_{2g}{}^3$ $e_g{}^2$) H.S $Fe^{III} = 5.6–6.1$ BM, LS ($t_{2g}{}^5$) $Fe^{III} = 1.8–2.1$ BM

[b] $\boldsymbol{\mu_{spin(M\text{-}L2\text{-}M`)}}$is spin magnetic moment for magnetically non-interacting metal ion pairs calculated using isolated spin states additive rule; $\mu_{spin} = g[S(S+1)]^{1/2}$, g is the gyromagnetic ratio = 2.0023; μ_{spin} for [Cu^{II}-L_2-Cu^{II}] = 1.73 + 1.73 BM; [Cu^{II}-L_2-Fe^{III} Cl] = 1.73 + 5.92 BM (HS Fe^{III}), 1.73 + 1.73 BM (LS Fe^{III}); μ-O-[Cu^{II}-L_2-Fe^{III}] = 5.92 + 5.92 BM (HS Fe^{III}- HS Fe^{III}); [Ni^{II}-L_2-Ni^{II}] = 2.83 + 2.83 BM; [Ni^{II}-L_2-Fe^{III} Cl] = 2.83 + 5.92 BM (HS Fe^{III}), 2.83 + 1.73 (LS Fe^{III}); μ-O-[Ni^{II}-L_2-Fe^{III}] = 5.92 + 5.92 (HS Fe^{III}- HS Fe^{III})

[c] $\boldsymbol{\mu_{eff} > \mu_{spin(M\text{-}L2\text{-}M`)}}$(magnetic enhancement, ferromagnetic coupling), $\boldsymbol{\mu_{eff} < \mu_{spin\ (M\text{-}L2\text{-}M`)}}$(magnetic quenching, antiferromagnetic coupling)

[d] Spin–spin interaction in these bimetallic macromolecular complexes

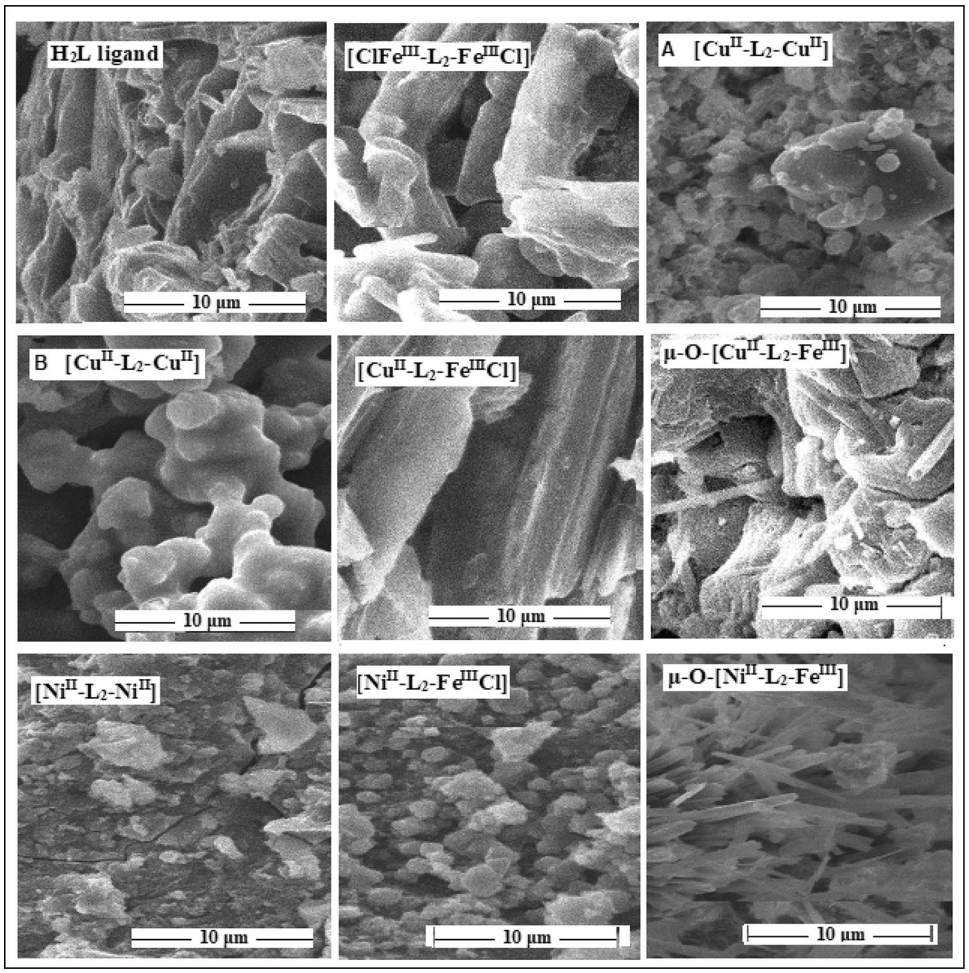

Fig. 6 SEM images of prepared H_2L ligand and the corresponding BMCs

magnetic quenching of (- 0.17 BM) suggests poor antiferromagnetic coupling between the [Fe^{III}-Fe^{III}] centers.

Since the magnetic sites in these BMCs are not located in close proximity to permit super exchange magnetic interactions as in -oxo, cyano and azido systems, the spin–spin interaction should have taken place via spin delocalization mechanism over the π-conjugated spacer [35–37]. In these homo-BMCs the phenylene π-spacer allows different degrees of antiferromagnetic interaction as indicated by Δμ. Since the spin–spin communication between the metal centers occur through the HOMO levels of the π-spacer, one can attribute the degree of magnetic coupling to the level of matching between the HOMO levels of the π-spacer and the redox energy levels of the metal sites involved [28]. The high antiferromagnetic interaction observed for [Cu^{II}-Cu^{II}] shows that the employed imine-oxime π-spacer facilitate spin delocalization in contrary to the inadequate magnetic exchange pathway seen in [Fe^{III}-Fe^{III}].

A close inspection of the magnetic data of the hetero-bimetallic chloro derivative of [Cu^{II}-L_2-$Fe^{III}Cl$] and [Ni^{II}-L_2-$Fe^{III}Cl$] BMCs shows that the Fe^{III} centers in both BMCs retain their LS state while they exhibit different M-M` interactions. Here, the π-conjugated spacer in [Cu^{II}-L_2-$Fe^{III}Cl$] allows magnetic quenching of (− 0.54) BM leading to aantiferromagnetic interaction on contrary of the [Ni^{II}-L_2-$Fe^{III}Cl$] analog where substantial magnetic enhancement is observed (+ 1.16) BM leading to ferromagnetic coupling. This unexpected observation invokes the notion that the spin mediating π-conjugated spacer utilizes different exchange orbitals for spin delocalization phenomenon.

On the other hand, the μ-oxo-[Cu^{II}-L_2-Fe^{III}] and μ-oxo-[Ni^{II}-L_2-Fe^{III}] exhibit large magnetic moments of 12.87 and 12.23 BM, respectively unlike their chloro precursors. The observed large values exceed what is expected for spin delocalization over the π-spacer in [M^{II}-HS Fe^{III}] pairs. The observed high μ_{eff} values of 12.87 and 12.23 BM allows super-exchange mechanism pathway to operate through the short μ-oxo bridged Fe^{III} centers on adjacent backbones causing the electronic configuration to adapt spin state in [HS Fe^{III}-**O**-HS Fe^{III}], Scheme 2. Here, magnetic enhancements of ($\mathbf{\Delta\mu} = 1.03$ and 0.39 BM) is observed in the μ-oxo-[Cu^{II}-L_2-Fe^{III}] and μ-oxo-[Ni^{II}-L_2-Fe^{III}], respectively.

Furthermore, the appreciable chain-chain separation of 3.2–3.6 Å as calculated from P-XRD combined with weak intermolecular forces makes one to conveniently conclude that the observed magnetic interaction is intramolecular in nature in the homo- and hetero bimetallic macromolecular complexes unless they are cross-linked via short bridge as μ-oxo, μ-cyano and μ-azido. Indeed, for efficient molecular magnets the magnetic sites should be linked in a proximity through small bridges [2, 29, 36, 38].

3.7 D.C. Current–Voltage (I-V) Characteristics

The electrical characteristics of the prepared BMCs was examined by passing a DC current through their compressed discs in a wide voltage range of 0–120 V. The current–voltage (I-V) data was divided and analyzed into a low voltage (0–20 V) and a high voltage (20–120 V) regime [24, 25]. The linear correlation between I and V in both voltage regimes can described by ohm`s Law (I = G V) where the slope gives the conductance (G) from which conductivity (σ) can be calculated (G = (σ x A)/L, where A and L are the area and thickness of the compressed disc). Typically, electronic conduction processes occur in the low-voltage regime (< 20 V) whereas at high voltage ionic conduction becomes operative which is not the case in the prepared BMC materials [24]. Here, it is evident from the DC data in Table 4 and the linear plots in Fig. 7 that the bi-nucleating ligand displays semiconducting properties ($2.4_{*}10^{-7}$ S.m^{-1}) with relatively large bandgap indicating ohmic conduction mechanism over the entire voltage range. In other words, the charge transfer is electronic with no contribution from the H^{+} of the oxime groups (=NOH).

Table 4 Solid state conductance (G), and conductivity (σ) of the prepared H_2L ligand, and the homo- and hetero-bimetallic macro complexes (BMCs)

BMCs	Conductance (G)[a] siemens	Thickness (L) mm	Conductivity (σ)[b] S m^{-1}
H_2L	$7.0_{*}10^{-8}$	0.458	$2.4_{*}10^{-7}$
[Cu^{II}-L_2-Cu^{II}]	$4.5_{*}10^{-9}$	0.771	$2.6_{*}10^{-8}$
[Ni^{II}-L_2-Ni^{II}]	$1.1_{*}10^{-7}$	0.687	$5.7_{*}10^{-7}$
[$ClFe^{III}$-L_2-$Fe^{III}Cl$]	$6.5_{*}10^{-10}$	0.664	$3.2_{*}10^{-9}$
[Cu^{II}-L_2-$Fe^{III}Cl$]	$1.1_{*}10^{-7}$	0.791	$6.5_{*}10^{-7}$
[Ni^{II}-L_2-$Fe^{III}Cl$]	$9.5_{*}10^{-8}$	0.479	$3.4_{*}10^{-7}$
μ-O-[Cu^{II}-L_2-Fe^{III}]	$8.5_{*}10^{-8}$	1.063	$6.8_{*}10^{-7}$
μ-O-[Ni^{II}-L_2-Fe^{III}]	$9.5_{*}10^{-8}$	0.665	$4.8_{*}10^{-7}$

[a]Radius 6.51 mm, Area (A) for all samples is 1.33×10^{-4} m^2

[b]σ = G $_{*}$ (L/A), L (thickness, m), A (area, m^2); σ = 10^{-16}-10^{-6} (insulator), 10^{-6}-10^{2} (semiconductor), 10^{2}–10^{8} Sm^{-1}(conductor)

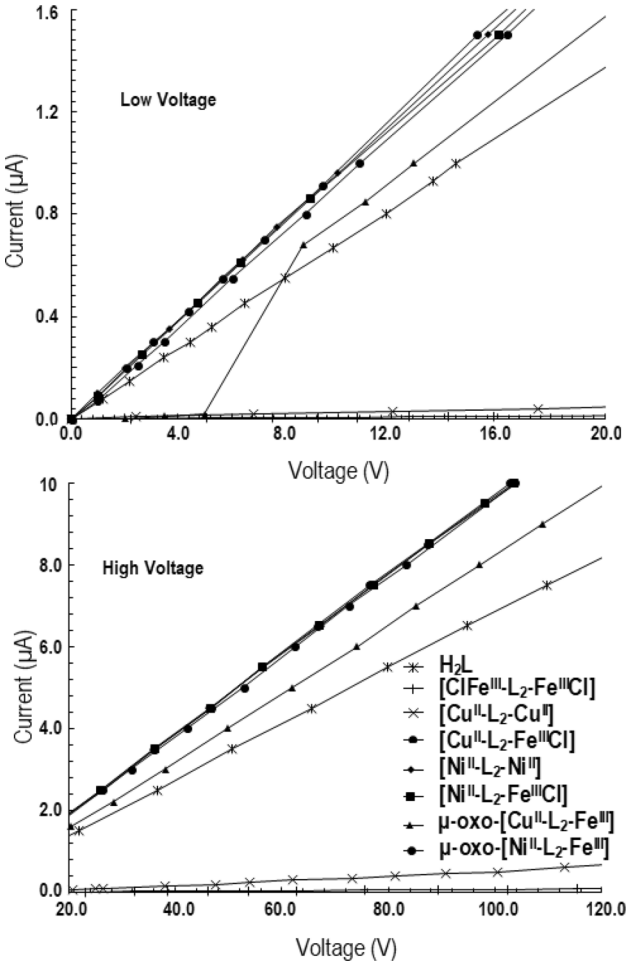

Fig. 7 I-V plot in the low voltage (0–20 V) and high voltage regimes (20–120 V) for the prepared H_2L ligand and the corresponding homo- and hetero- BMCs

Similarly, the observed linear relation is also evident in all BMCs thus indicating electronic conduction no contribution from ionic conduction. The absence of ionic participation clearly suggests that the ligated Cl in [Cu^{II}-L_2-$Fe^{III}Cl$], [Ni^{II}-L_2-$Fe^{III}Cl$] and [$ClFe^{III}$-L_2-$Fe^{III}Cl$] is held tightly within the coordination sphere of the Fe^{III}. A close inspection of the Fig. 7 and electrical conductivity data in Table 4 shows that the homo- BMCs [Cu^{II}-L_2-Cu^{II}] and [$ClFe^{III}$-L_2-Fe^{III}] exhibit lower conductivity than the free backbone ligand (H_2L) of about 1–2 order of magnitude. The role of paramagnetic metal centers in hindering electron hopping across the backbone is evident in both the low and high conduction regimes. Interestingly, the μ-O-[Cu^{II}-L_2-Fe^{III}] in the low voltage regime behaves like these two BMCs but rapidly jump 5–8 V to behave like the other four BMCs showing relatively higher conductivity of about 1 order than the bi-nucleating ligand backbone.

A close look at the minor role of metal types and their oxidation state in homo- and hetero-bimetallic on charge

hopping invokes the notion that electronic transport proceeds by hopping between the π-conjugated segments in the backbone. In other words, this conclusion applies in the homo-metallic BMCs where charge hopping occurs between similar electronic states as well as in the hetero-metallic where the charge transport proceeds by electron hopping between different energy states. Furthermore, despite the large increase in magnetic properties, chain-chain packing variation and morphology modifications seen in μ-oxo-[M^{II}-L_2-Fe^{III}] species relative to their chloro precursors, no clear enhancement/ hindering in their electrical conductivity is observed. This observation clearly suggests that intramolecular electron hopping predominates with no practical conduction between the chains [24, 34].

3.8 Flexible Magneto-responsive Thin Films

The magnetic behaviors of soluble discrete molecular and macromolecular ferromagnetic materials provide crucial components in the development of magnetic thin films, membranes, ferro-fluids and other magnetic composites [37–40]. In this respect, paramagnetic metal-containing macromolecular systems constitute a relatively new class of materials for applications in stimuli-responsive magnetic and photomagnetic thin films and spintronic devices. These magnetic systems are generally fabricated by dispersing very fine magnetic particles into polymeric materials to afford the desired composite. Such dispersion process often results in aggregation /agglomeration of the magnetic particles leading to the deterioration of the magnetic properties especially when exposed to heat. In addition, the insolubility of the magnetic particles limits the threshold amounts that can be dispersed and therefore the magnetic properties of the magneto composites. These two major disadvantages can be overcome when using soluble molecular/ macromolecular magnets such as the one described here.

The ferromagnetic behavior, and appreciable solubility of the μ-oxo-[M^{II}-L_2-Fe^{III}] (where M^{II} = Cu^{II}, Ni^{II} in polar organic solvents motivated us to form magnetic thin films by solvent casting from DMSO/THF containing polymethylmethacrylate (PMMA). The solubility, well-organized rod texture and compatibility of the μ-oxo-[Ni^{II}-L_2-Fe^{III}] ferromagnetic material with the transparent PMMA matrix gave us a hand on forming magnetic microscopic thin films (~ 100 μm). Optical microscopic inspection of the obtained thin films shows some clustering of un-dissolved particles. The responsive functional properties of the obtained film were preliminarily examined by looking at its the magnetic characteristic in response towards stimulus Lab magnet and exposure to intense LED light, Fig. 8. This thin film exhibits a reversible brown-green photo-chromic property in LED light that may be tentatively attributed to introducing tetragonal distortion at the Ni^{II} sites in μ-oxo-[Ni^{II}-L-Fe^{III}] particles. These stimulus responsive properties are currently under further detailed investigation.

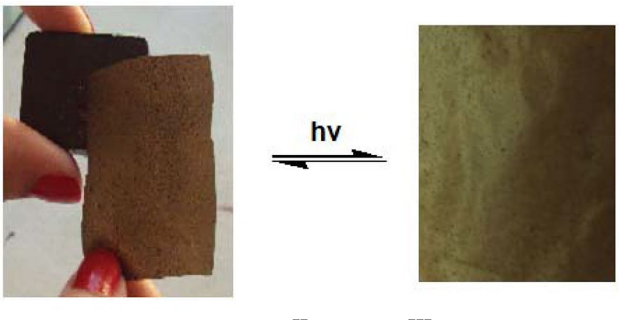

Fig. 8 Photograph of a thin film of μ-oxo-[Ni^{II}-**L_2**-Fe^{III}] magnetic BMC in PMMA matrix and its photochromic properties (color change from brown-green in UV light)

4 Conclusions

The ability of π-conjugated ligands to form macromolecular complexes offer versatile metal–organic network systems to examine multi-functional properties in materials. Deep understanding of the ability of π-conjugated organic spacers to transport electronic charge and control spin delocalization between paramagnetic metal centers is essential for developing new spintronic devices. The structural, optical, electrical, and magnetic properties inherited in the prepared regime demonstrate that the examined semiconducting π-spacer has clear ability to delocalize spin thus offering a favorable magnetic exchange pathway between the paramagnetic metal sites. Their solubility in polar organic solvents gives this class of macromolecules an advantage over the dispersion method in the fabrication of magneto-flexible membranes/ thin films as preliminarily demonstrated in this study. Our work is currently extended to exploit μ-oxo-[Fe^{II}-**L_2**-Fe^{III}] magnetic BMC in making magneto elastic thin films/ membranes. Herein, the appreciable photo absorption in the UV region of this magnetic thin films allow further examination of their photo-magnetism.

Acknowledgements The financial support from the Jordan University of Science and Technology is deeply appreciated (Grant No. 116/2009).

References

1. Y. Wang, D. Astruc, A.S. Abd-El-Aziz, Chem. Soc. Rev. **48**, 558 (2019)
2. J.M. Seco, I. Oyarzabal, S.P. Yáñez, J. Cepeda, A.R. Diéguez, Inorg. Chem. **55**(21), 11230 (2016)
3. S.M. Jansze, K. Severin, Acc. Chem. Res. **51**(9), 2139 (2018)

4. K.S. Mali, N. Pearce, S.D. Feyter, N.R. Champness, Chem. Soc. Rev. **46**, 2520 (2017)
5. C. Bizzarri, E. Spuling, D.M. Knoll, D. Volz, S. Bräse, Coord. Chem. Rev. **373**, 49 (2018)
6. C. Rüttiger, H. Hübner, S. Schöttner, T. Winter, G. Cherkashinin, B. Kuttich, B. Stühn, M. Gallei, A.C.S. Appl, Mater. Interfaces **10**(4), 4018 (2018)
7. M.P. Suh, Y.E. Cheon, E.Y. Lee, Coord. Chem. Rev. **252**, 1007 (2008)
8. J. Zhou, G.R. Whittell, I. Manners, Macromolecules **47**(11), 3529 (2014)
9. A.A.G. Valdivia, S.P. Yáñez, J.A. García, B. Fernández, J. Cepeda, A.R. Diéguez, Sci. Rep. (2020). https://doi.org/10.1038/s41598-020-65687-6
10. B. Wang, M. Jacquet, K. Wang, K. Xiong, M. Yan, J. Courtois, G. Royal, New J. Chem. **42**, 7823 (2018)
11. R.M. Clarke, T. Storr, Dalton Trans. **43**(25), 9380 (2014)
12. Z. Shao, X. Han, Y. Liu, W. Xu, Q. Wu, Q. Xie, Y. Zhao, H. Hou, Dalton Trans. **48**, 6191 (2019)
13. X. Pan, X. Wang, X. Wang, Y. Li, G. Liu, H. Lin, CrystEngComm **21**, 6472 (2019)
14. C.D. Mekuimemba, F. Conan, A.J. Mota, M.A. Palacios, E. Colacio, Inorg. Chem. **57**(4), 2184 (2018)
15. J.L. Wang, Y. Bai, H. Pan, G.S. Zheng, D.B. Dang, Dalton Trans. **46**, 12771 (2017)
16. B. Belhadji, L. Bergqvist, R. Zeller, P.H. Dederichs, K. Sato, H.K. Yoshida, J. Phys. **19**, 436227 (2007)
17. M.A. Halcrow, *Spin Crossover Materials: Properties and Applications* (John Wiley & Sons Ltd, Oxford, UK, 2013)
18. G. Fornasieri, A. Bordage, A. Bleuzen, Eur. J. Inorg. Chem. **259**, 1322 (2018)
19. X. Li, X. Wu, Z. Li, J. Yang, J.G. Hou, Nanoscale **4**, 5680 (2012)
20. V. R-Giménez, S. Tatay, C. M-Gastaldo 2020 Chem. Soc. Rev. DOI. 10.1039/C9CS00594C
21. L. Sun, C.H. Hendon, S.S. Park, Y. Tulchinsky, R. Wan, F. Wang, A. Walsh, M. Dincă, Chem. Sci. **8**(6), 4450 (2017)
22. C. Mathonière, Eur. J. Inorg. Chem. **3**(4), 248 (2018)
23. P. Blake, J. St. Onge, T-C. Chen, A. Langlois, A. Younus, I J. Hai, B-H Lin, Y-C Chiu, S. R-Gagné 2020 J. Mater. Chem. C. 8, 24, 8213
24. I. Arafa, H. El-Ghanem, S. Nemrat 2007 In Recent Developments in Polymer Research, A.V. Hopper (eds) Nova Science Publishers Inc., New York, pp 1–28.
25. I.M. Arafa, H. El-Ghanem, R. Al-Shalabi, J. Inorg. Organomet. Polym. **13**, 69 (2003)
26. W. Plass, Coord. Chem. Rev. **253**, 2286 (2009)
27. S. Ross, T. Weyhermüller, E. Bill, E. Bothe, U. Flörke, K. Wieghardt, P. Chaudhuri, Eur. J. Inorg. Chem. **5**, 984 (2004)
28. B.J. Holliday, T.M. Swager, Chem. Commun. **23**(36), 23 (2005)
29. T.A. Shestimerova, A.V. Shevelkov, Russ. Chem. Rev. **87**, 28 (2018)
30. X. Ma, E.A. Suturina, S. De, P. Négrier, M. Rouzières, R. Clérac, P. Dechambenoit, Angew. Chem. **57**(26), 7841 (2018)
31. S. Gupta, M. Fátima, C.G. da-Silva, A.J.L. Pombeiro, Heliyon **5**(5), e01623 (2019)
32. C.I. Yang, Z.Z. Zhang, S.B. Lin, Coord. Chem. Rev. **289**, 289–290 (2015)
33. D.S. Bolotin, N.A. Bokach, VYu. Kukushkin, Coord. Chem. Rev. **313**, 62 (2016)
34. J.W. Maciel, L.H.G. Kalinke, A.K. Valdo, F.T. Martins, R. Rabelo, N. Moliner, J. Cano, M. Julve, F. Lloret, D. Cangussu, J. Braz. Chem. Soc. **30**(11), 2413 (2019)
35. C. Gatti, G. Macetti, L.L. Presti, Acta. Cryst. **B73**, 565 (2017)
36. D.J.R. Brook, C. Fleming, D. Chung, C. Richardson, S. Ponce, R. Das, H. Srikanth, R. Heindl, B.C. Noll, Dalton Trans. **47**, 6351 (2018)
37. J.R. Kumpfer, S.J. Rowan, J. Am. Chem. Soc. **133**, 12866 (2011)
38. M.B. Zakaria, A.A. Belik, T. Nagata, T. Takei, S. Tominaka, T. Chikyow, J. Mag. Mag. Mater. **486**, 165276 (2019)
39. P. Borys, Z.J. Grzywna, J. Memb. Sci. **445**, 107 (2013)
40. A. Sohail, M. Fatima, R. Ellahi, K.B. Akram, J. Molecular Liquids **285**, 47 (2019)